Solar Phys (2016) 291:1159–1171
DOI 10.1007/s11207-016-0881-6

Relationship Between Sunspot Rotation and a Major Solar Eruption on 12 July 2012

Rui Wang[1] · Ying D. Liu[1] · Thomas Wiegelmann[2] · Xin Cheng[1,3] · Huidong Hu[1] · Zhongwei Yang[1]

Received: 23 July 2015 / Accepted: 12 March 2016 / Published online: 5 April 2016

Abstract We present an analysis of *Solar Dynamics Observatory* (SDO) observations of an X1.4 class flare on 12 July 2012 (SOL2012-07-12T15:37L082C105), which was associated with a pronounced sunspot rotation in the associated active region. Based on the magnetograms taken with the *Helioseismic and Magnetic Imager* (HMI) on the SDO, we measured the rotational speed of the sunspot. We also used a technique, called the differential affine velocity estimator for vector magnetograms (DAVE4VM), to determine the horizontal velocities and the magnetic helicity flux transport. The helicity flux rate due to shearing motion changed sign after the onset of the eruption. A high correlation between the sunspot rotation speed and the change in the total accumulated helicity was found. We also calculated the net fluxes of the respective magnetic polarities and the net vertical currents. The net current in the region of interest showed a synchronous change with the sunspot rotation rate. The magnetic configurations of the sigmoid filament in the active region and the associated possible interaction between different structures were further investigated by means of a nonlinear force-free field extrapolation. We identified a possible magnetic reconnection region from the three-dimensional magnetic fields and its association with EUV structures. These results suggest that the major eruption of this active region was connected with the sunspot rotation.

Keywords Active regions, magnetic fields · Flares, dynamics · Magnetic helicity · Sunspots, magnetic fields

✉ Y.D. Liu
liuxying@spaceweather.ac.cn

1 State Key Laboratory of Space Weather, National Space Science Center, Chinese Academy of Sciences, Beijing 100190, China

2 Max-Planck-Institut für Sonnensystemforschung, Justus-von-Liebig-Weg 3, 37077 Goettingen, Germany

3 School of Astronomy and Space Science, Nanjing University, Nanjing 210093, China

1. Introduction

Possible trigger mechanisms of solar eruptions including solar flares and coronal mass ejections (CMEs) have been discussed extensively in previous studies. It is commonly believed that the trigger mechanisms mainly consist of three types, *i.e.*, shearing motions, flux emergence, and magnetohydrodynamic (MHD) instabilities. Hagyard *et al.* (1984) found that both magnetic shear and field strength are strongest at the onset of a flare and suggested that the flare is triggered when the magnetic shear stress exceeds some critical value. A flare is triggered mostly along a polarity inversion line (PIL), not perpendicular to it (Schmieder *et al.*, 1996). Flux emergence has also been found to play a significant role in triggering solar flares. A filament interacting with the new flux that emerges nearby in an orientation favorable for magnetic reconnection is likely to erupt (Feynman and Martin, 1995; Chen and Shibata, 2000). In recent years, as more and more high-resolution photospheric vector magnetograms became available, kink and torus instabilities of the magnetic field as an important trigger mechanism have been given more attention. For example, Török and Kliem (2004) have performed three-dimensional (3D) MHD simulations of a kink-unstable flux rope that match the observed EUV structures well.

Sunspot rotation has been suggested to be one of the efficient mechanisms for injecting magnetic helicity or magnetic energy into active regions. Observations of sunspot rotations were first carried out a century ago by Evershed (1910). As more sophisticated instruments appeared, this type of rotational motion has become associated with the trigger mechanism of solar eruptions. Brown *et al.* (2003) provided observational evidence that suggested that the cause of the observed rotation of sunspots might be photospheric flows or twisted flux tube emergence. Zhang, Liu, and Zhang (2008) suggested that the rotational motions not only transport the magnetic energy and complexity, but also play a key role in the onset of homologous flares. More recently, Kazachenko *et al.* (2009) and Vemareddy, Ambastha, and Maurya (2012) indicated that sunspot rotation can be the most dominant contributor to the twist, helicity, and energy of the magnetic field. The rotational motions may have some relations to the evolution of the flux rope system, which eventually erupts and forms a CME (Ruan *et al.*, 2014). Vemareddy, Ambastha, and Maurya (2012) also showed that the peak rotation rate of the sunspot coincided with the occurrence of major eruptive events using the constructed azimuth-angle *vs* time intensity maps. Modeled sunspot rotation has been used in numerical simulations to trigger an eruption by Tokman and Bellan (2002), Török and Kliem (2003), and Török *et al.* (2013). Török *et al.* (2013) demonstrated that a rotating sunspot in their numerical MHD model triggered an eruption by inflating the field passing over a preexisting flux rope, thereby weakening the stabilizing downward tension force of the overlying field.

On 12 July 2012, active region (AR) NOAA 11520, which is the same active region that produced the extreme solar storm on 23 July (Liu *et al.*, 2014), spawned an X1.4 flare (SOL2012-07-12T15:37L082C105) with a fast halo CME (Dudík *et al.*, 2014; Cheng *et al.*, 2014; Möstl *et al.*, 2014; Hess and Zhang, 2014). In previous studies, Dudík *et al.* (2014) and Cheng *et al.* (2014) both indicated that there was a high-lying flux rope structure in addition to a sigmoid filament, which was observed in an XUV wavelength only for a short time before the eruption. Cheng *et al.* (2014) called the structure consisting of the sigmoid filament and high-lying flux rope a "double-decker" and suggested that the high-lying flux rope fully erupted, whereas the lower flux rope did not erupt or erupted only partially. Although the event has been studied in some detail, there is still much to explore. One of the most prominent features of this event is the fast rotation of a sunspot before the eruption. It is worth noting that the footpoints of both the high- and low-lying flux rope

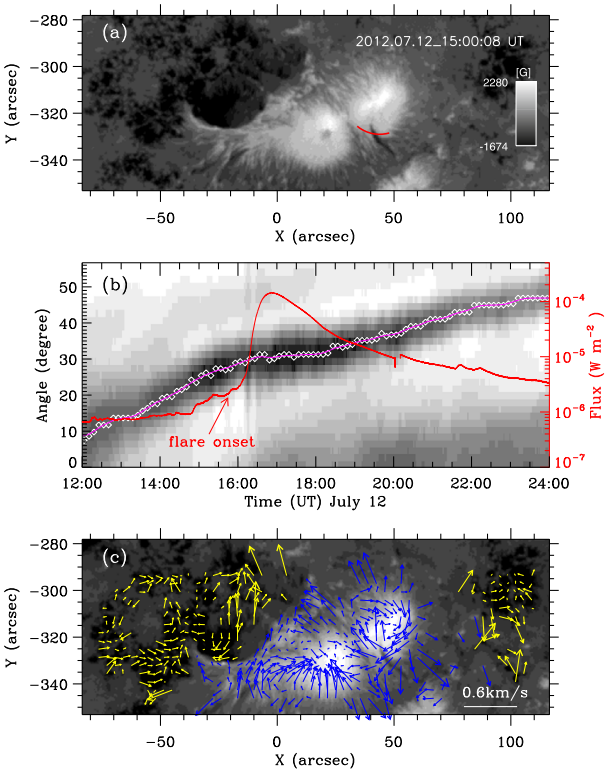

Figure 1 (a) The HMI magnetogram for NOAA AR 11520 observed at 15:00 UT on 12 July 2012. The red curve shows the slice position across a black tongue that we use as a tracking target. The color bar indicates the intensity of the photospheric magnetic field along the line of sight. (b) The angle-time stack plots of the rotating sunspot along the slice. The GOES X-ray flux in the 1 – 8 Å channel is overplotted as the red curve. (c) The vertical component of the vector magnetogram overlaid by the velocity field at the photosphere around 15:00 UT. The velocity fields on the positive (white) and negative (black) vertical magnetic field components are represented by blue and yellow arrows, respectively, with a length scale of 0.6 km s^{-1} shown by the white bar.

structures were rooted near this rotating sunspot. There might be some relation between the rotational motion and the eruption.

We here use data from the *Helioseismic and Magnetic Imager* (HMI; Schou *et al.*, 2012) onboard the *Solar Dynamics Observatory* (SDO; Pesnell, Thompson, and Chamberlin, 2012) to investigate the relation between the sunspot rotation and the major eruption on 12 July 2012. We also determine the magnetic topological structures using a nonlinear force-free field (NLFFF) extrapolation technique and compare the results with the EUV images from the *Atmospheric Imaging Assembly* (AIA; Lemen *et al.*, 2012) on SDO to understand the effect of the sunspot rotation. The results obtained here are of importance for understanding the relationship between sunspot rotations and solar eruptions.

2. Observations and Analysis

The HMI instrument provides high time-resolution magnetograms with a 45 s cadence and vector magnetic field data with a 12 min cadence for NOAA AR 11520 (Hale class $\beta\gamma\delta$). The spatial resolution is $0''.5$ per pixel. In this investigation, we employed the Lambert cylindrical equal area projection and remapped the vector magnetic field data (Gary and Hagyard, 1990; Calabretta and Greisen, 2002; Thompson, 2006). The X1.4 flare started at 15:37 UT, peaked at 16:49 UT, and ended at 17:30 UT. More than 1 h was needed from the onset of the flare to its peak time, which is unusually long for flare eruptions (see the soft X-ray light curve in Figure 1).

2.1. Evolution of the Rotating Sunspot

We traced the AR from 12:00 UT to 23:59 UT on 12 July 2012. The umbra of the positive-polarity sunspot was bisected by a light bridge. The western portion of the sunspot, *i.e.*, west of the light bridge, exhibited an obvious clockwise rotation, as shown in Figure 1a. To quantify its angular speed, we used a black magnetic tongue as the tracking object (similar to the analysis by Ruan *et al.*, 2014), which swept the strongest rotation region where the major coronal structures anchored. To cover the whole trajectory of the magnetic tongue during the investigated time, a 57° arc slice along the direction of the sunspot rotation is presented. The center of the semicircle is approximately at the center of the sunspot rotation. Then we stacked these slices from 480 successive magnetograms for 12 h and obtained the angle-time plot (see Figure 1b). We picked up the minimum intensities in each slice (corresponding to the black magnetic tongue) and plotted them with small squares, which were then smoothed and connected by a purple line. The angle of the magnetic tongue started from about 7° around 12:00 UT and ended at about 47° around 23:59 UT, which means that the sunspot rotated about 40° during 12 h. The average angular speed was $\approx 3^\circ\ \mathrm{h}^{-1}$. Before 16:00 UT, the average angular speed was $\approx 6^\circ\ \mathrm{h}^{-1}$. During the eruption the rotational motion almost stopped, and then it started again after 18:30 UT with an average angular speed of $\approx 2^\circ\ \mathrm{h}^{-1}$. The magnetic tongue showed a radial motion directed toward the sunspot center during the eruption instead of smooth rotation (which can be seen from the animation of the sunspot rotation). It seems that the rotational motion was disrupted by the eruption and then recovered after the eruption, but with a slower rotational speed.

Figure 1c shows the transverse velocities of flux elements in the photosphere around 15:00 UT, which were determined by applying a differential affine velocity estimator for vector magnetograms (DAVE4VM; Schuck, 2008) to the HMI vector magnetograms. Clearly, the flows were clockwise across the magnetic tongue. The flow of the magnetic flux around the rotating sunspot was a joint effect of flux emergence and shearing motion. The eastern part of the positive-polarity sunspot showed flow convergence without obvious rotational motion. Furthermore, the shearing motions along the PIL (the region between the yellow and blue arrows) were not as strong as the sunspot rotation during this period.

2.2. Time Evolution of the Helicity Flux Injection and the Vertical Current

Sunspot rotation is generally thought to be related to the injection of magnetic helicity, and it may provide processes of both flux emergence and shearing motion. Therefore, a correlation between the magnetic helicity and the sunspot rotation may be found. Because we lack information on the magnetic field in the corona, we cannot measure magnetic helicity directly from the data, but we can obtain an approximate relative magnetic helicity through the photospheric magnetograms. The relative magnetic helicity flux transport (helicity flux transport hereafter) across a surface S can be expressed as (Berger and Field, 1984)

$$\left.\frac{\mathrm{d}H}{\mathrm{d}t}\right|_S = \left[\int_S 2(\mathbf{B}_\mathrm{t}\cdot\mathbf{A}_\mathrm{p})v_z\,\mathrm{d}S\right] + \left[\int_S -2(\mathbf{v}_\mathrm{t}\cdot\mathbf{A}_\mathrm{p})B_z\,\mathrm{d}S\right], \tag{1}$$

where $\mathbf{A}_\mathrm{p}$ is the vector potential of the potential field on the photosphere. The first term on the right-hand side of this equation represents the helicity flux transport through the passage of the helical field lines through the photospheric surface (*i.e.*, emergence of new flux), and the second term corresponds to the helicity flux transport through the shuffling horizontal motion of the field lines on the surface (*i.e.*, shearing motions). The vector potential can be uniquely determined by the observed photospheric vertical magnetic field B_z with a fast Fourier transform method, as implemented by Chae (2001).

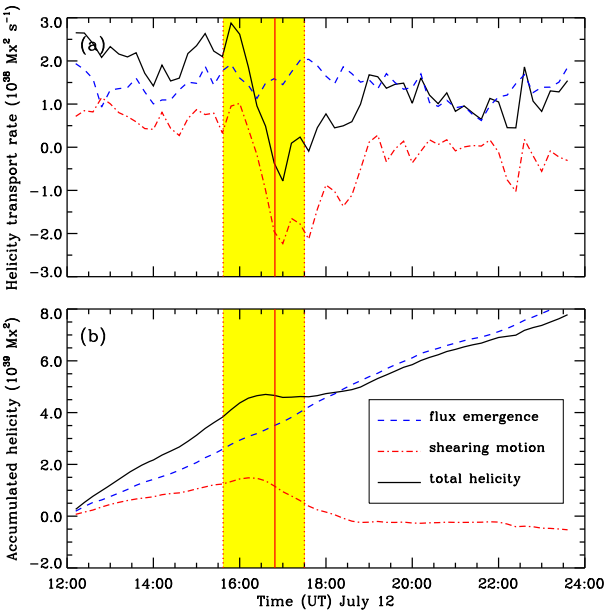

Figure 2 Helicity flux transport (a) and accumulated magnetic helicity (b) as a function of time. The vertical yellow squares in both panels correspond to the interval of the eruption, and the red solid line indicates the flare peak time. The blue, red, and black curves represent the helicity from flux emergence, helicity from shearing motion, and the total helicity, respectively.

Figure 2a shows the helicity flux transport as a function of time, which was obtained by the DAVE4VM method (Liu and Schuck, 2012; Vemareddy, 2015). The window size used in the DAVE4VM method is 19 pixels, which was determined by examining the Pearson correlation, Spearman rank order correlation, and the slope between $\nabla_h \cdot (v_z \mathbf{B}_t - \mathbf{v}_t B_z)$ and $\delta B_z/\delta t$ (Schuck, 2008). The helicity flux transport due to the shearing motions of the photospheric magnetic field kept a little lower positive value than that from flux emergence before the eruption. However, it changed sign after the eruption onset and showed a sudden drop around 16:12 UT. It reached a negative peak value after the flare maximum, which is approximately -2×10^{38} Mx^2 s^{-1} (Mx: maxwell). Then it recovered, but remained lower than its pre-eruption level. The helicity flux transport due to flux emergence did not change much during the eruption compared with that from the shearing motion of the photospheric magnetic field. The total helicity flux transport (the sum of the two) also went through an abrupt change from positive to negative during the eruption and then recovered to some extent after the eruption.

Figure 2b shows the accumulated magnetic helicity, which was obtained by integrating the measured helicity flux transport ($\mathrm{d}H/\mathrm{d}t$) from the start of the observing run to the specified time. The accumulated helicity from flux emergence increased smoothly with an almost constant growth rate, whereas the accumulated helicity from shearing motions decreased during the eruption. The total accumulated helicity first increased until around 16:12 UT, then stayed flat until around 19:00 UT, and finally rose again, but with a slower rate than before the eruption. These results indicate that the rate of change in the magnetic helicity during the eruption was dominated by the shearing motion of the photospheric magnetic field and not by flux emergence.

We note that the evolution of the total accumulated magnetic helicity (the black curve in Figure 2b) seems similar to the trend of the sunspot rotation (the purple curve in Figure 1b). Therefore, we performed a correlation analysis between these two parameters. As expected, the correlation coefficient is 0.995, which most likely indicates a close relation between the sunspot rotation and the magnetic helicity. We note that the helicity is calculated based on

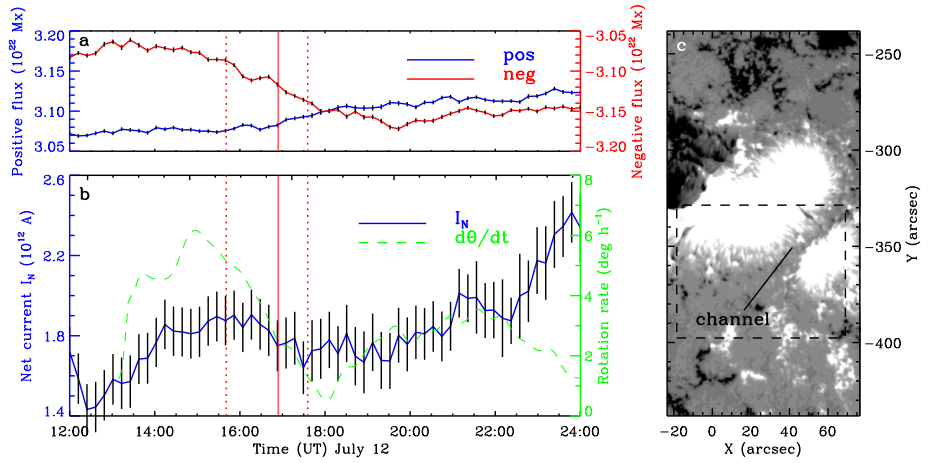

Figure 3 Time evolution of magnetic flux over the entire AR and the net current in the local region. Panel (a) shows the integrated magnetic fluxes of the positive (blue) and negative (red) polarities, respectively. The vertical dotted lines bracket the interval of the flare eruption, and the red solid line indicates the flare peak time. Panel (b) shows the net vertical currents I_N (blue line) of the positive polarity and sunspot rotation rate (green dashed line), respectively. Panel (c) shows the region (in the black dashed box) for calculating the net current on the vertical component of the vector magnetogram. The uncertainties of the magnetic flux and net current are shown by the black error bars.

the vector magnetograms of the *whole* AR. This implies that the rotation of only one single sunspot probably dominated the rate of change in the magnetic helicity of the whole active region.

To ensure that the eruption was exclusively related to the sunspot rotation and not to the flux emergence, we investigated the time evolution of the net flux of the magnetic polarity in the whole AR as shown in the top panel of Figure 3. The net flux is computed as

$$\Phi = \sum_{i=0}^{N} B_z \Delta x \Delta y, \tag{2}$$

which follows the practice of Vemareddy, Venkatakrishnan, and Karthikreddy (2015), where Δx and Δy are the dimensions of the pixels. We considered pixels with magnetic fields greater than 50 gauss (G) in the computation of the net flux B_z distribution. The error limit of the net flux is estimated as

$$\delta\Phi = \sqrt{\sum_{i=0}^{N} (\delta B_z)_i^2 \Delta x \Delta y}. \tag{3}$$

The integrated vertical magnetic fluxes of positive (Φ_p) and negative polarity (Φ_n) are represented by blue and red solid curves in Figure 3a, respectively. The positive flux contains the flux from the rotating sunspot. Before the eruption, Φ_p and Φ_n were at almost the same magnitude around 3.07×10^{22} Mx. During the eruption, both Φ_p and Φ_n increased, and the amplitude of Φ_n became greater than Φ_p. However, the variations in of Φ_n were lower than 3 %, and Φ_p variations were only around 1 %. The relative changes of the fluxes of both polarities are small during the eruption. The emergence of the magnetic flux therefore probably did not play an important role compared to the sunspot rotation in the major eruption.

We also calculated the net vertical currents as Vemareddy, Venkatakrishnan, and Karthikreddy (2015) implemented,

$$I = \sum_{i=1}^{N} (J_z)_i \Delta x \Delta y, \tag{4}$$

where the current density $J_z = \frac{1}{\mu_0}(\frac{\partial B_y}{\partial x} - \frac{\partial B_x}{\partial y})$ can be estimated by summing over N pixels in the region of interest. Furthermore, the error limit of the current over a region of interest is estimated as

$$\delta I = \sqrt{\sum_{i=0}^{N} (\delta J_z)_i^2} \Delta x \Delta y, \tag{5}$$

where

$$(\delta J_z)_{i,j} = \frac{1}{\mu_0} \frac{\sqrt{(\delta B_x)_{j-1}^2 + (\delta B_x)_{j+1}^2 + (\delta B_y)_{i-1}^2 + (\delta B_y)_{i+1}^2}}{2\Delta x}. \tag{6}$$

Figure 3b shows the time evolution of the net vertical current I_N of the positive (N) polarity and the sunspot rotation rate $d\theta/dt$. The region of interest for calculating the net current is shown in Figure 3c. As most of the region of interest is covered by positive polarity and the net current I_S of the negative (S) polarity has almost the same trend but much lower magnitude than I_N, I_S is not presented here. Figure 3c shows that there was a channel between the main rotating sunspot and another positive polarity. As the magnetic tongue swept this narrow region in a clockwise direction, an irregular flow may have formed along the channel, and the magnetic field might have become more complicated in this region. Moreover, the footpoints of some major magnetic structures were located here, which raises the question whether there were some obvious changes in the net current in this region according to Vemareddy, Venkatakrishnan, and Karthikreddy (2015), who studied the relation between the net currents and the eruptive events. As we expected, there was a relatively fast increase in the net current before the eruption; it increased by 35 % (I_N by $1.4-1.9 \times 10^{12}$ A). For the sake of comparison, we plot the rotation rate $d\theta/dt$ in Figure 3b. The net current is seen to increase until the beginning of the eruption, similar to the rotation rate profile. The sunspot rotation slowed down during the eruption, accompanied by a decrease in the net current. Then the sunspot rotation rate recovered a little to decrease again, while the net current continued to increase. Their discrepancy at the end of the day is thought to be caused by the uncertainty in the measurements of the rotation rate, since the magnetic tongue became diffuse at the later time of the rotation (see Figure 1b).

According to these results, we suggest the following scenario for the eruption. The sunspot rotated at relatively high speed before the eruption, while the total accumulated helicity of the whole AR and the net current increased until around 16:12 UT. The X1.4 flare entered into its impulsive phase and a CME lifted off. The rotational motion of the sunspot almost stopped, at the same time the helicity flux rate changed its sign, and the net current also decreased. The sudden stop of the sunspot rotation and turnover of sign of helicity flux rate may be related by means of the helicity release by the CME, the untwisting of the magnetic field configuration, or the flux motions reported by Vemareddy, Ambastha, and Maurya (2012). After about 18:30 UT, the sunspot rotation recovered, and the helicity and the net current correspondingly increased again. To summarize, the sunspot rotation with the total accumulated helicity of the whole region and the net current of the region of interest changed in a synchronous manner.

2.3. Extrapolated Magnetic Field Topology and the EUV Images

Here we examine the coronal magnetic field configuration to better understand the relation between the sunspot rotation and the eruption. We obtained the coronal magnetic field by adopting the NLFFF method as proposed by Wheatland, Sturrock, and Roumeliotis (2000) and extended by Wiegelmann (2004) and Wiegelmann and Inhester (2010). We used the NLFFF code, which has been optimized for application to SDO/HMI vector magnetograms (Wiegelmann *et al.*, 2012) to extrapolate the coronal field from the observed vector magnetograms in a Cartesian domain. A pre-processing procedure (Wiegelmann, Inhester, and Sakurai, 2006) was employed to remove most of the net force and torque from the data, so that the boundary can be more consistent with the force-free assumption. In addition, the overall magnetic flux is imbalanced due to the limited size of vector magnetograms. It might in principle be better to always choose a magnetogram such that the majority of the flux is centered on the analyzed domain. By means of the pre-processing, the vector magnetograms can be approximately flux balanced. This extrapolation technique has been successfully applied in our previous analyses on two successive solar eruptions (Wang *et al.*, 2014) and the CME channeling (Wang *et al.*, 2015), and it performed well for investigating the relationship between the magnetic flux rope along the PIL and the solar filament (Guo *et al.*, 2010). For the extrapolation, we binned the data to about $1''.0$ per pixel and adopted a computation domain of $256 \times 256 \times 160$ grids.

To check how well the force-free criterion of the resulting NLFFF field was fulfilled, we present some quality evaluation results here. Wiegelmann *et al.* (2012) used the parameters $L1$ and $L2$ to check the $\mathbf{J} \times \mathbf{B} = 0$ and $\nabla \cdot \mathbf{B} = 0$ conditions in the full computational box, respectively. Here, these two parameters are 0.60 and 0.40, respectively. They should be as small as possible (for ideal NLFFF they must be zero). Values below 5 are considered to be good, but values below 1 are better. The sine of the current-weighted average angle σ_j (see Wiegelmann *et al.*, 2012) between the extrapolated magnetic field and the electric current is 7.14°. It should also be as small as possible, but up to about 10° is acceptable. Finally, we checked the energy compared with the energy of the potential field. The ratio between the NLFFF energy and that of the potential field (*i.e.*, E_{nff}/E_{pot}) is 1.22, which is also acceptable (see the comparison results between different extrapolation methods by Metcalf *et al.*, 2008).

Figure 4 shows a set of sample field lines from the resulting NLFFF extrapolation at 16:12 UT, which exhibit most of the extrapolated magnetic topological structures of this AR. One of the most prominent features of the magnetic topological structures is the S-shaped magnetic structure surrounding the positive-polarity sunspots, which consists of a flux rope structure along the PIL ending at the rotating sunspot and some short magnetic loops. Figure 5a shows the main coronal magnetic configuration around the flare source region (as shown in Figure 4) from the SDO view at 16:12 UT. The SDO/AIA 171 Å image is used as the background. We note that at 16:12 UT the flare entered its impulsive phase (see Figure 1b) and a high-lying hot channel started to expand and rise, resulting in an energetic CME. Combining this with a lateral view of the coronal magnetic field topology (see Figure 5b), we can see that the magnetic flux rope structure lies along the PIL and under a slightly twisted loop structure. Both the flux rope and the overlying loop have an end rooted near the rotating sunspot. The flux rope and the overlying loop might be interacting. We envision that the rotational motion of the sunspot was likely to shear the footpoints of the field lines, which may have led to interactions between the low-lying flux rope and the overlying loop. A similar study by Vemareddy and Wiegelmann (2014) suggested that the line-tied footpoint motions can perturb the fan-spine system and cause null-point reconnection. The helicity flux rate and net vertical current derived in Section 2.2 show synchronous changes

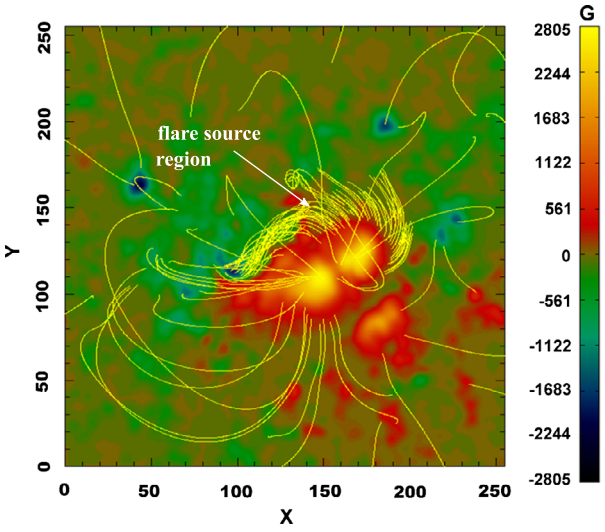

Figure 4 A set of sample field lines from the NLFFF extrapolation at 16:12 UT. The vertical and horizontal axes show the computed area of 256 × 256 grids. The vertical component of the pre-processed photospheric vector magnetogram is shown as the background, whose levels are indicated by the color bar on the right-hand side.

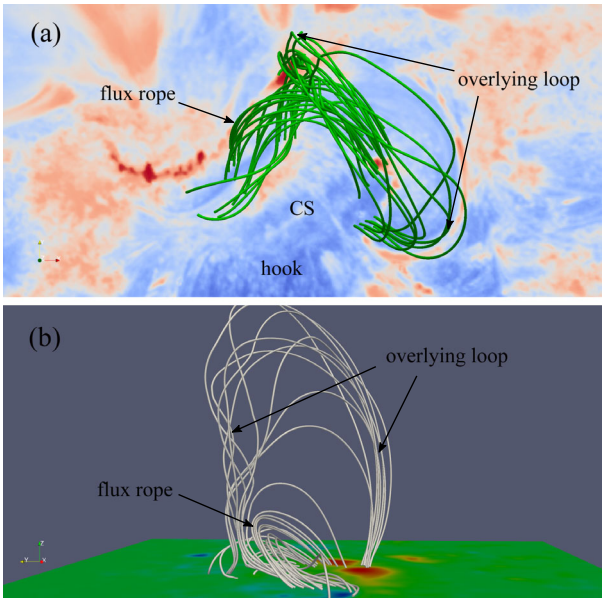

Figure 5 (a) Coronal magnetic topology around the flare source region based on the NLFFF extrapolation superposed on the SDO/AIA 171 Å image at 16:12 UT. (b) Magnetic topology as seen from a side view with the vertical component of the pre-processed photospheric vector magnetogram on the bottom boundary. Positive polarity of the magnetic field is coded in red and negative polarity in blue.

with the sunspot rotation rate. The net current already had increased significantly before the eruption. The appearance of the net current indicates a possible change in the field connectivity (Vemareddy, Venkatakrishnan, and Karthikreddy, 2015). Therefore the current sheet may have been built during the course of the sunspot rotation, where reconnection possibly ensues at the onset of the eruption.

To investigate how the low-lying flux rope interacted with its overlying loop, we examined the distributions of J/B (*i.e.*, currents normalized by the magnetic field strength), which can help us identify the places where magnetic reconnection is likely to occur (Fan and Gibson, 2007). Figure 6a shows the 2D distribution of J/B along the red dashed line

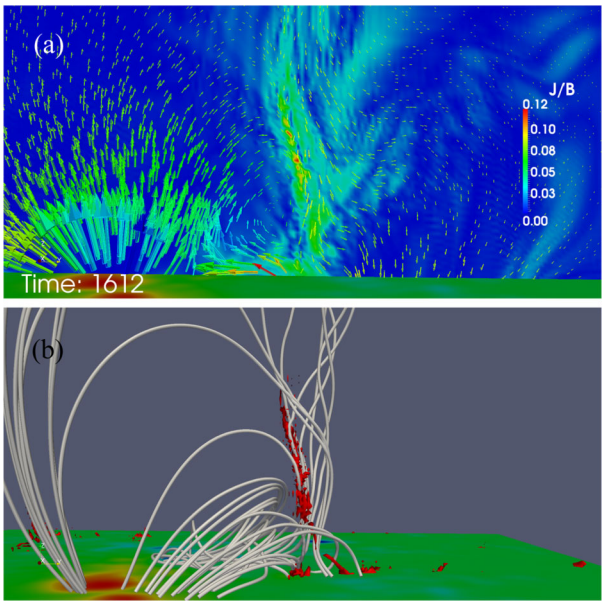

Figure 6 (a) 2D color image of J/B showing the location of a possible magnetic reconnection region. The rough position of its cross section is marked as the red dashed line (CS) in Figure 5a. The arrows show the direction and strength of the magnetic field. (b) A 3D rendering of the J/B iso-surface at 0.07 mA G^{-1} (solid red) with the magnetic field lines. The format is the same as in Figure 5b.

(CS) in Figure 5a. A possible narrow magnetic reconnection region can be seen along the interface between the low-lying flux rope structure with clockwise poloidal fields and its overlying loop. A 3D rendering of the J/B iso-surface at 0.07 mA G^{-1} and magnetic field lines is displayed in Figure 6b. Comparison between the 2D distribution and 3D rendering provides more confidence that magnetic reconnection is likely to occur along the interface between the flux rope and the overlying loop. The formation of the reconnection region is likely to be caused by the interaction between these two different magnetic structures as a result of the sunspot rotation.

We next compared the extrapolated magnetic topology with EUV images. The EUV observations at 171 Å show a low-lying sigmoid filament (see Figure 7a). The extrapolated S-shaped magnetic structure in Figure 4 is consistent with the filament channel. The low-lying flux rope structure in the S-shaped magnetic structure lies along the eastern part of the sigmoid filament, and one end of the overlying loop appears consistent with the hook of the filament (also see Figure 5a). Comparing the 3D magnetic topology with the EUV images, we also find that the spatial location of the possible narrow magnetic reconnection region between the low-lying flux rope and the overlying loop is consistent with the EUV brightening at 16:12 UT (as indicated by the blue dashed box in Figure 7b), which rapidly expanded and evolved into the following major flare. The tip of the hook structure (as indicated by the red dashed box) was located near the rotating sunspot and was moving along the sunspot rotation direction. It is worth noting that another high-lying flux rope structure was observed as a hot channel at 94 Å (as shown by the red dashed line in Figure 7c) in addition to the two main structures mentioned above. The high-lying flux rope is much more extended than the extrapolated overlying loop, therefore they could be two different structures. Figure 7c shows that both the low-lying filament channel (yellow dashed line) and the high-lying hot channel have their ends near the rotating sunspot (as indicated by the purple dashed circle). The high-lying hot channel appeared at 14:00 UT, started to expand at 16:12 UT, and finally erupted, which can be seen only at 94 Å. The high-lying hot channel probably produced the CME. However, the high-lying hot channel cannot be reconstructed with the NLFFF

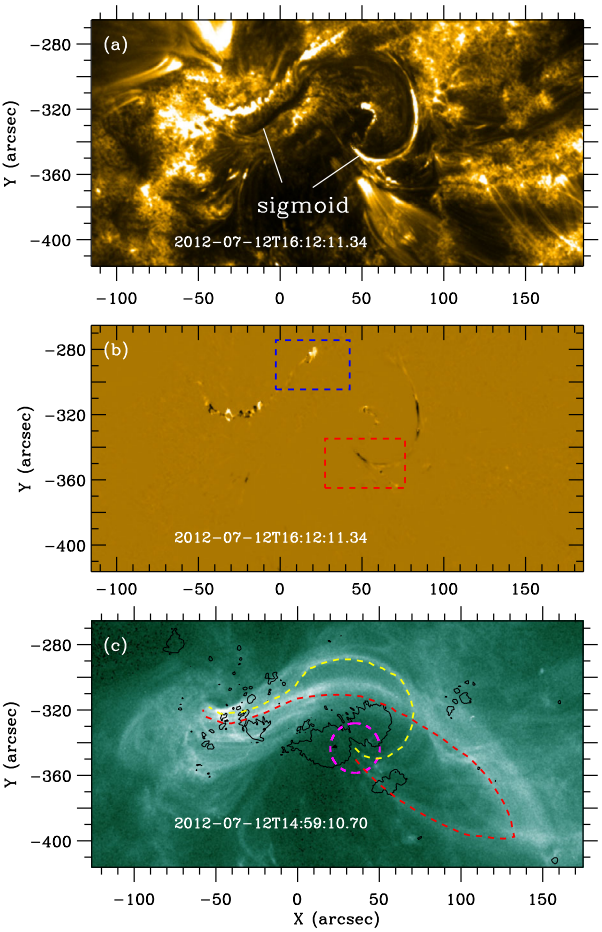

Figure 7 (a) A low-lying sigmoid filament seen in the AIA 171 Å image at 16:12 UT. (b) Running-difference image of 171 Å at the same time. The blue box indicates the EUV brightening and the red box marks the hook of the filament. (c) The low-lying filament and high-lying hot channel seen in the 94 Å image marked by the yellow and red dashed lines, respectively. The purple circle indicates the positions of their footpoints of interest. Contours of ± 1000 G of the photospheric magnetic field along the line of sight are also overlaid on the EUV image and marked in black.

method. A possible cause is that this erupting hot channel was very dynamic and therefore cannot be reconstructed with a static NLFFF model.

Based on these results (*i.e.*, the synchronous behavior between the rotational speed of the sunspot, the magnetic helicity and net current of the region of interest, the connection between the flux ropes and the loop to the rotating sunspot, and the consistency of the extrapolated magnetic topology with the observed EUV images), the sunspot rotation may have sheared the footpoints of the photospheric magnetic fields, which eventually resulted in the eruption. The sunspot rotation may also have caused the low-lying flux rope to interact with the overlying loop, leading to the formation of a possible magnetic reconnection region between them. Interestingly, the low-lying flux rope and its overlying loop survived the eruption. The high-lying hot channel visible only at 94 Å erupted into the CME.

3. Summary

We investigated AR 11520, which produced an X1.4 flare and an energetic CME on 12 July 2012. Different from previous studies of this event, we focused on the rotation of the

sunspot, which was a prominent feature associated with the eruption, as revealed by the HMI magnetograms. We used the DAVE4VM method to calculate the horizontal velocity of the magnetic field on the photosphere, and furthermore obtained the magnetic helicity flux transport and the accumulated helicity. The sign of the helicity flux rate due to the shearing motion was changed after the onset of the eruption. The change rate of the total accumulated helicity in the whole active region has a very high correlation with the angular speed variation of the sunspot rotation. We also calculated the net fluxes of the magnetic polarities and the net vertical currents in a local region nearby the rotating sunspot. The net vertical current changed in a synchronous manner with the sunspot rotation. It increased until the beginning of the eruption, when the sunspot rotation rate had already reached its peak value. Taking these together, the rotational motion was probably very closely related with the major eruption.

Then we compared the extrapolated coronal magnetic configuration with the associated EUV images before the eruption. We determined the coronal magnetic field structures by means of the NLFFF extrapolation. The extrapolated S-shaped magnetic structure around the rotating sunspot is consistent with a low-lying sigmoid filament channel. Around the flare source region, the reconstruction shows a low-lying flux rope as part of the S-shaped magnetic structure and a loop overlying the flux rope. The extrapolated flux rope lies along the eastern part of the sigmoid filament, while one end of the overlying loop appears to agree with the hook of the filament. At the onset of the flare around 16:12 UT, the EUV images exhibited a brightening and motions of the EUV loop footpoints. We investigated the possible interaction region between the flux rope and its overlying loop where magnetic reconnection was likely to occur, which could be connected with the sunspot rotation. We found that the spatial location of the EUV brightening at 171 Å in the flare kernel is consistent with the interface between the low-lying flux rope structure and its overlying loop. The observed hook structure showed a motion along the direction of sunspot rotation. The extrapolated low-lying flux rope, its overlying loop, and another observed high-lying hot channel at 94 Å that finally erupted all had their ends rooted near the rotating sunspot. The sunspot rotation may have sheared the footpoints of these structures and caused magnetic reconnection along the interface between the low-lying flux rope and the overlying loop, which most likely resulted in the flare and CME.

Acknowledgements The work was supported by the Specialized Research Fund for State Key Laboratories of China, NSFC under grant 41374173, and the Recruitment program of Global Experts of China.

References

Berger, M.A., Field, G.B.: 1984, *J. Fluid Mech.* **147**, 133.
Brown, D.S., Nightingale, R.W., Alexander, D., Schrijver, C.J., Metcalf, T.R., Shine, R.A., Title, A.M., Wolfson, C.J.: 2003, *Solar Phys.* **216**, 79.
Calabretta, M.R., Greisen, E.W.: 2002, *Astron. Astrophys.* **395**, 1077.
Chae, J.: 2001, *Astrophys. J. Lett.* **560**, L95.
Chen, P.F., Shibata, K.: 2000, *Astrophys. J.* **545**, 524.
Cheng, X., Ding, M.D., Zhang, J., Sun, X.D., Guo, Y., Wang, Y.M., Kliem, B., Deng, Y.Y.: 2014, *Astrophys. J.* **789**, 93.
Dudík, J., Janvier, M., Aulanier, G., Del Zanna, G., Karlický, M., Mason, H.E., Schmieder, B.: 2014, *Astrophys. J.* **784**, 144.
Evershed, J.: 1910, *Mon. Not. Roy. Astron. Soc.* **70**, 217.
Fan, Y., Gibson, S.E.: 2007, *Astrophys. J.* **668**, 1232.
Feynman, J., Martin, S.F.: 1995, *J. Geophys. Res.* **100**, 3355.
Gary, G.A., Hagyard, M.J.: 1990, *Solar Phys.* **126**, 21.

Guo, Y., Schmieder, B., Démoulin Wiegelmann, T., Aulanier, G., Török, T., Bommier, V.: 2010, *Astrophys. J.* **714**, 343.
Hagyard, M.J., Teuber, D., West, E.A., Smith, J.B.: 1984, *Solar Phys.* **91**, 115.
Hess, P., Zhang, J.: 2014, *Astrophys. J.* **792**, 49.
Kazachenko, M.D., Canfield, R.C., Longcope, D.W., Qiu, J., Des Jardins, A., Nightingale, R.W.: 2009, *Astrophys. J.* **704**, 1146.
Lemen, J.R., Title, A.M., Akin, D.J., Boerner, P.F., Chou, C., Drake, J.F., *et al.*: 2012, *Solar Phys.* **275**, 17.
Liu, Y., Schuck, P.W.: 2012, *Astrophys. J.* **761**, 105.
Liu, Y.D., Luhmann, J.G., Kajdič, P., Emilia, K.J., Lugaz, N., Nitta, N.V., *et al.*: 2014, *Nature Commun.* **5**, 3481.
Metcalf, T.R., De Rosa, M.L., Schrijver, C.J., Barnes, G., van Ballegooijen, A.A., Wiegelmann, T., Wheatland, M.S., Valori, G., McTtiernan, J.M.: 2008, *Solar Phys.* **247**, 269.
Möstl, C., Amla, K., Hall, J.R., Liewer, P.C., De Jong, E.M., Colaninno, R.C., *et al.*: 2014, *Astrophys. J.* **787**, 119.
Pesnell, W.D., Thompson, B.J., Chamberlin, P.C.: 2012, *Solar Phys.* **275**, 3.
Ruan, G., Chen, Y., Wang, S., Zhang, H., Li, G., Jing, J., *et al.*: 2014, *Astrophys. J.* **784**, 165.
Schmieder, B., Démoulin, P., Aulanier, G., Golub, L.: 1996, *Astrophys. J.* **467**, 881.
Schou, J., Scherrer, P.H., Bush, R.I., Wachter, R., Couvidat, S., Rabello-Soares, M.C., *et al.*: 2012, *Solar Phys.* **275**, 229.
Schuck, P.W.: 2008, *Astrophys. J.* **683**, 1134.
Thompson, W.T.: 2006, *Astron. Astrophys.* **449**, 791.
Tokman, M., Bellan, P.M.: 2002, *Astrophys. J.* **567**, 1202.
Török, T., Kliem, B.: 2003, *Astron. Astrophys.* **406**, 1043.
Török, T., Kliem, B.: 2004, In: Walsh, R.W., Ireland, J., Danesy, D., Fleck, B. (eds.) *Proceedings of the SOHO 15 Workshop – Coronal Heating*, *ESA*, **SP-575**, 56.
Török, T., Temmer, M., Valori, G., van Driel-Gesztelyi, L., Vršnak, B.: 2013, *Solar Phys.* **286**, 453.
Vemareddy, P.: 2015, *Astrophys. J.* **806**, 245.
Vemareddy, P., Wiegelmann, T.: 2014, *Astrophys. J.* **792**, 40.
Vemareddy, P., Ambastha, A., Maurya, R.A.: 2012, *Astrophys. J.* **761**, 60.
Vemareddy, P., Venkatakrishnan, P., Karthikreddy, S.: 2015, *Res. Astron. Astrophys.* **15**, 1547.
Wang, R., Liu, Y.D., Yang, Z., Hu, H.: 2014, *Astrophys. J.* **791**, 84.
Wang, R., Liu, Y.D., Dai, X., Yang, Z., Huang, C., Hu, H.: 2015, *Astrophys. J.* **814**, 80.
Wheatland, M.S., Sturrock, P.A., Roumeliotis, G.: 2000, *Astrophys. J.* **540**, 1150.
Wiegelmann, T.: 2004, *Solar Phys.* **219**, 87.
Wiegelmann, T., Inhester, B.: 2010, *Astron. Astrophys.* **516**, A107.
Wiegelmann, T., Inhester, B., Sakurai, T.: 2006, *Solar Phys.* **233**, 215.
Wiegelmann, T., Thalmann, J.K., Inhester, B., Tadesse, T., Sun, X., Hoeksema, J.T.: 2012, *Solar Phys.* **281**, 37.
Zhang, Y., Liu, J., Zhang, H.: 2008, *Solar Phys.* **247**, 39.